Fuyong Wang (Orcid ID: 0000-0003-1202-5283)
Jiuyu Zhao (Orcid ID: 0000-0001-9867-1395)
Jianchao Cai (Orcid ID:0000-0003-2950-888X)

# 3D Tight Sandstone Digital Rock Reconstruction with Deep Learning

**Jiuyu Zhao[1], Fuyong Wang[1, 2, *], Jianchao Cai[1]**

[1] *State Key Laboratory of Petroleum Resources and Prospecting, China University of Petroleum* (*Beijing*), *Beijing 102249*

[2] *Unconventional Petroleum Research Institute, China University of Petroleum* (*Beijing*) *Beijing 102249*

Corresponding author: Fuyong Wang (wangfuyong@cup.edu.cn)

**Key Points:**

- Reconstructing 3D heterogeneous tight sandstone digital rock based on DCGAN with 3D convolution used in the generator and the discriminator.
- A more comprehensive method for evaluating reconstructed 3D digital rock with strong heterogeneity is adopted.
- The reconstructed 3D digital rock has the similar porosity distribution with the original heterogeneous tight sandstone.

## Abstract

Tight oil and gas reservoirs have attracted many attentions and are one of the hottest research fields in recent years. Tight sandstones have complex pore structures and narrow pores and throats with pore sizes varying from nanometers to micrometers, studying flow mechanisms in tight sandstones is of significance to tight oil/gas reservoir development. Reconstructing the digital rock which can comprehensively represent petrophysical properties of tight sandstone is the key to simulate the fluid flow in micro/nano pores. This paper proposes a new method of reconstructing 3D digital rock from CT image of tight sandstones based on a deep convolutional generative adversative network (DCGAN), and 3D convolution in the generator and discriminator are adopted to realize reconstruction from one dimensional data to 3D digital rock model. Studies show that when the training effect is slightly poor, the generated digital rock model will have noise, which can be reduced by post-processing; when the training effect is well, DCGAN can accurately reconstruct the 3D digital rock of tight sandstones, the reconstructed digital rock is very consistent in pore size, geometric structure, and connectivity of natural tight sandstones. When multiple 3D tight sandstone CT images are used for training, the DCGAN can learn the pore structure characteristics of entire tight sandstones, and the porosity distribution obtained from generated digital rock are similar to original tight sandstones.

**Keywords:** digital rock; tight sandstone; generative adversarial neural network; deep learning

## 1 Introduction

Unconventional oil and gas are important alternative energy in the future (Jia, 2017). Tight oil/gas reservoirs in China are mainly continental deposits, and a great deal of micro and nano-pores are widely developed with poor connections, complex structures and strong heterogeneity (Yao et al., 2013; Li et al., 2017; Wang et al., 2019) , therefore, the seepage mechanisms in tight oil/gas reservoirs are quite complicated. It is necessary to study the microscopic flow mechanism and figure out its influencing factors for developing the tight oil/gas reservoirs efficiently and economically. Digital rock is an advanced technology to study the physical properties and flow behaviors insides of sedimentary rock (Berg et al., 2017), which will play an important role in the exploration and development of tight oil/gas reservoirs.

In order to investigate the characteristics of sedimentary rock, the key is constructing a 3D digital rock model which can accurately characterize the pore structure of micro and nano-pores. At present, the methods of 3D digital rock reconstruction can be divided into two main categories: physical experiments and numerical reconstructions (Yao et al., 2013). Physical experiments have to use a high-resolution scanning instruments, these methods are time consuming with high cost (Izadi et al., 2017). The common physical experiments methods includes serial sectioning, magnetic resonance imaging (MRI) (Ouellette et al., 2015), X-ray computed tomography (Elbakri and Fessler, 2002), focused ion beam (FIB)-scanning electron microscopy (SEM) (Bera et al., 2011), and etc. Numerical reconstruction method reconstructs digital rock with computer based on the statistical information of pore structures, and can be divided into two categories: random field method and process-based method (Øren and Bakke, 2002). The random field method also has multiple types, including Gaussian random field method(Yuan et al., 2010), simulated annealing method (Yeong and Torquato, 1998), Markov chain Monte Carlo Method (Wu et al., 2004), sequential indicator simulation method (Keehm et al., 2004) and multiple-point statistics method(Lei, 2020), and etc.

Recently, artificial intelligent has been gradually widely applied in oil industry, including seismic data processing and interpretation (Cao and Wu, 2017; Imamverdiyev and Sukhostat, 2019), well drilling (Chen et al., 2019; Noshi and Schubert, 2018), oil and gas exploitation (Ahmadi and Chen, 2019; Li et al., 2019). It is a trend that the whole oil industry will pay more attentions on intelligent system development. Generative adversarial networks (GAN) is a neural network model proposed by Goodfellow et al. (Goodfellow et al., 2014), which can capture the distribution of data and generate a data sample consistent with the distribution of real data. The main ideal of GAN is derived from the zero-sum game in game theory, the generator can learn the distribution of data through the continuous game between the generator and the discriminator, which can produce an output that is more consistent with real data. It has been widely used in intelligent fusion(Ma et al., 2019), intelligent generating(Wang et al., 2018), super-resolution reconstruction(Bulat et al., 2018), classification(Zhou et al., 2018), etc. It also has been used in the construction of 3D psychical models, such as face model (Gecer et al., 2019; Gecer et al., 2019), bed/chair/table model (Li et al., 2019), archaeological objects (Hermoza and Sipiran, 2018).

As mentioned above, the GAN provides a new method for digital rock reconstruction, and different GAN model has been used in digital rock reconstruction. Mosser et al (Mosser et al., 2017; Mosser et al., 2018) firstly introduced GAN to reconstruct digital rock. They generated a 3D digital rock model (64×64×64) , and used autocorrelation function to evaluate the reconstructed digital rock, but the process of model training is time consuming. DCGAN adapts the convolutional neural network (CNN) as the generator and discriminator, which is very good at dealing with image processing problem (Radford et al., 2015). In 2018, Guan (2018) used DCGAN to generate 2D images rather than 3D models, and another GAN model, Wasserstein GAN (Arjovsky et al., 2017), was introduced for comparison in their presentation. Liu et al.(Liu et al., 2019)used Berea sandstone (64×64×64) and Estaillades carbonate (128×128×128) binary data respectively to train DCGAN model and for 3D digital rock reconstruction; Shams et al.(2020) coupled GAN and auto-encoder neural network (AE) for reconstructing a porous media with inter-grain and intra-grain pores. The function of GAN is producing 3D porous media (64×64×64) with inter-grain pores, and the AE (256×256) is to generate intra-grain pore in the images outputted from the GAN. Valsecchi et al.(Valsecchi et al., 2020)designed the generator with 3D convolution and the discriminator with 2D convolution for generating a 3D model with 2D image stacks output (64×64), and three types of brainy image data was used to validate the model by two-point probability function and Minkowski functionals. The conditional generative confrontation network (CGAN) (Mirza and Osindero, 2014), which adds constraints to the original GAN by introducing a conditional variable ‘y’ into the generative model and the discriminant model to guide the generation of data, is another model for digital rock reconstruction. Feng et al.(2019a; 2019b) applied CGAN to reconstruct complete 2D core images (128×128) based on less information of images and real core data. Volkhonskiy et al.(2019)added autoencoders before the generator of CGAN to extract pore structure information and input it to the generator as constraints, and different natural core samples were used to evaluate its performance but the consuming time of generative model training is about 10 hours.

Digital rock reconstruction with GAN is an emerging technology, there are many challenges need to overcome, such as a long training time, complex model, small size of generated model, and representativeness, generalization ability and interpretability are still weak. In this paper, a new method of digital rock reconstruction based on DCGAN is developed, and the 3D convolution networks are adopted in the generator and discriminator of DCGAN. The CT

images of tight sandstones form Yanchang formation, Ordos Basin, NW China are used to validate the newly proposed model. The geometry and connectivity of pores in the reconstructed digital rocks are analyzed with three case studies.

## 2 Methodology

### 2.1 GAN

As a classical unsupervised learning model, GAN combines the game theory and deep neural network, has some advantages those generative models don't have. It avoids inference during training, and can produce a clearer sample. If the discriminator is well trained, the generator can learn the distribution of data perfectly in theory by training. The value function of GAN $V(D,G)$ is defined as (Goodfellow et al., 2014):

$$\min_G \max_D V(D,G) = E_{x\sim p_{data}(x)}\left[\log D(x)\right] + E_{z\sim p_z(z)}\left[\log\left(1-D\left(G(z)\right)\right)\right] \quad (1)$$

where $x$ is the real data; $z$ is the noise; $p_{data}(x)$ is the distribution of real data; $p_z(z)$ is the distribution of noise; $G(z)$ is the output of generator; $D(x)$ represents the probability that $x$ is real data judged by the discriminator.

In the training process, backpropagation algorithm is used to optimize the parameters of network. When the distribution of real data and the distribution of generator is equal, the value function is the lowest, and the generative model can perfectly learn the data distribution. In order to avoid the generator falling into local minima, the discriminator will train several times while the generator updates once.

DCGAN scales up GAN using CNN, and three changes were made to the structure and activation function of CNN. First, the pooling layer in conventional CNN is replaced by convolution. Then, the generator uses ReLU activation for all layers except the output layer, which uses tanh activation, but the discriminator uses Leaky ReLU activation in all layers. Finally, both the generator and the discriminator apply batch normalization for stabilizing training.

### 2.2 Network architecture

The schematic diagram of applying DCGAN for 3D digital rock reconstruction is shown in **Figure 1**, and the detail parameters of discriminator and generator are shown in **Table 1**.

The discriminator is a CNN model to discriminate the input data is real data or the data from generator. It has four convolutional layers, and each convolutional layer consists of a batch normalization layer with momentum of 0.8, a drop layer with loss ratio of 0.25, and the Leaky ReLU with activation of 0.2. The last layer is a fully connect layer, its activation is sigmoid function. The structure of discriminator is shown in **Figure 2**.

The generator receives a random noise conforming to normal distribution, and converts the random noise to a 1D vector by a fully connect layer, then reshapes the random noise to a four-dimensional vector. Three up sampling layers are used to enlarge the 3D images, the followed convolutional layer of each up sampling layer can learn the kernel by training, and then the data flows into batch normalization layer and ReLU activation. The last layer is a

convolutional layer, and the activation function is tanh function. The momentum of batch normalization layer is set to 0.8. The structure of the generator used in this manuscript is shown in **Figure 3**.

## 3 Data and plateform

### 3.1 Data sets

As shown in **Figure 4**, the Micro XCT-510 scanner was used to obtain the CT images of tight sandstones Yanchang formation, Ordos Basin, NW China. The resolution of CT images is 1.22 μm.

There are always some noises in the CT images due to the influence of equipment, environment, and the minerals of the rock itself. The image noises have significant influences on pore structure analysis, thus the image preprocessing must be conducted. The common methods of image denoising includes Gaussian filter, median filter, adaptive Wiener filter, mean filtering, and wavelet thresholding(Buades et al., 2005; Zhang and Desai, 2002). Here the median filter was used to remove the noise in CT images. After that, the images will be divided into pore and matrix two parts, and binary image can reduce the calculation time comparing with grey images.

Considering the calculation ability of our computer, the data for training was sub-sampled from the binary CT images. Binary CT images for training (32×32×910) are shown in **Figure 5**, the black is the pore and the gray is the matrix. According to the statistics of porosity of 910 core slices, the binary images with porosity less than 10% account for 60% of total CT images, indicating that most pores are small pores, which reflects strong heterogeneity of tight sandstone pore structures. The 2D images must to be transform into 3D data, and the normalization of binary data (0~255) also are also needed. The range of data after normalization is between -1 and 1 because the distribution of the tanh function ranges from -1 to 1.

### 3.2 Platform

Several platforms have been developed for machine learn, such as Tensorflow (Abadi et al., 2016), Keras (Gulli and Pal, 2017), Caffe (Jia et al., 2014), Pytorch (Paszke et al., 2017), Theano(Al-Rfou et al., 2016). In this paper, Keras is used to build the DCGAN model, which is an advanced neural network API written in Python and be coupled with Tensorflow or Theano as the backend. As the network has a complex structure and needs a large amount of calculation, the configuration of computer will have a great impact on the training and application of deep learning. A computer with a single NVIDIA GTX 1050 GPU was used in this paper.

## 4 Results and discussion

### 4.1 Case 1

The input data is 3D binary image with the size of 32×32×32, and the value function of the generator and the discriminator are optimized by Adam method. The learning rate is set to 0.002, the exponential decay rate for the moment estimation is 0.5, the number of training epoch is 6000, and the batch data size is 1. The generated digital rock by is shown in **Figure 6**. Compared with the original digital rock, the generated digital rock has similar pores, but some isolated pores are also generated. Compared 9 pores in the original digital rock, there are 30 pores in the generated digital rock. **Figure 7** shows the distribution of pore area and pore volume

of original digital rock and generated digital rock, which can be found that most of pores in the generated digital rock is the small pores.

Removing all the isolated small pores with the pore volume less than 5 $\mu m^3$ in the generated digital rock, only 9 large pores are left, which are same to the pores in the original digital rock. As shown in **Table 2**, the barycenter coordinates of the pores in the generated digital rock are very close to those in original rock, except for the pores nos. 1, 6, and 7. For other pores, the distances between the generated pores and original pores are less than 1 μm. In addition, the distributions of pore volumes and pore areas in the original digital rock and generated digital rock are very close, as shown in **Figure 8**.

Two-point probability function can reflect the pore distribution insides of digital rock. As shown in **Figure 9**, the curves of two-point probability functions of the original digital rock and generated digital rock are very close to each other, which can demonstrate that the method of digital rock reconstruction based on deep learning is reliable, and can accurately reconstruct digital rock. The porosity of original rock and generated digital rock is about 4.5%, but the porosity of generated digital rock is a little higher, due to there are several isolated small pores in the generated digital rock. Even that, the reconstructed digital rock by deep learning can accurately represent the original digital rock.

### 4.2 Case 2

The input data is another 3D binary images with size of 32×32×32, and the original digital rock is shown in **Figure 11(a)**. Using the parameters of DCGAN obtained from training above, the generated digital rock reconstructed by deep learning is shown in **Figure 11(b)**. As shown in **Table 4**, the barycenter coordinates of the pores in the original digital rock and generated digital rock are the same.

As shown in **Figure 11**, the porosity of the original digital rock and generated digital rock is 46.8%, and the curves of two-point probability functions of the original digital rock and generated digital rock coincide. It could be concluded that a well-trained DCGAN can generate the same digital rock as the original input dataset.

### 4.3 Case 3

Different from only 32 slices of CT images used in case 2, total 910 slices of CT images are used for training DCGAN. The initial parameters for GCGAN are same to those in cases 1 and 2, except the batch size in case 3 is 4 rather than 1. It means that four digital rocks with the size of 32×32×32 are used as the input data for DCGAN training, and also four digital rock with the size are generated. **Figure 13** shows the four digital rocks generated by DCGAN after training. As the original digital rock with the size of 32×32×910 has strong heterogeneity, and the size of generated digital rock is different from the original digital rock, the two-point probability function is not suitable for comparing the difference of pore size distribution between generated digital rock and original digital rock. As shown in **Figure 13**, the distribution of area porosity in 2D images of the four generate digital rocks (32×4 slices) is similar to that in the original digital rock (910 slices). The images with porosity between 0% and 10% both account for about 60% of total images, and the small pores account for a larger proportion.

## 5 Conclusions

This paper proposed a new method of reconstructing 3D digital rock based on deep learning, and the DCGAN with 3D convolution in generator and discriminator is built for 3D digital rock reconstruction. The reconstructed digital rock is evaluated by the statistical results of pore size distribution and two-point probability function. The results show when DCGAN is well trained, it can generate a representative digital rock similar to original one. When the DCGAN is not well trained, the post processing such as image filtering can improve the accuracy of digital rock reconstruction. The well-trained DCGAN can generate the digital rock with different pore structures, but the porosity distribution is similar to the original digital rock. The reconstructed digital rock is helpful for study the characteristics of pore structures and flow mechanism insides of porous media. The future work can focus on improving the accuracy of reconstructed digital rock, reducing training time, strengthening model generalization ability, and model explanation and evaluation.

## Acknowledgments

This work was supported by National Natural Science Foundation of China (No. 51874320). The data used in this paper will be freely available online through Mendeley Data (http://dx.doi.org/10.17632/ksdj6j9c2g.1).

## References

Abadi, M. et al., 2016. Tensorflow: Large-scale machine learning on heterogeneous distributed systems. *arXiv preprint* arXiv:1603.04467.

Ahmadi, M.A. and Chen, Z., 2019. Machine learning models to predict bottom hole pressure in multi-phase flow in vertical oil production wells. *The Canadian Journal of Chemical Engineering*, 97(11): 2928-2940. https://doi.org/10.1002/cjce.23526

Al-Rfou, R. et al., 2016. Theano: A Python framework for fast computation of mathematical expressions. *arXiv e-prints*: arXiv: 1605.02688.

Arjovsky, M., Chintala, S. and Bottou, L., 2017. Wasserstein gan. *arXiv preprint* arXiv:1701.07875.

Bera, B., Mitra, S.K. and Vick, D., 2011. Understanding the micro structure of Berea Sandstone by the simultaneous use of micro-computed tomography (micro-CT) and focused ion beam-scanning electron microscopy (FIB-SEM). *Micron*, 42(5): 412-418. https://doi.org/10.1016/j.micron.2010.12.002

Berg, C.F., Lopez, O. and Berland, H., 2017. Industrial applications of digital rock technology. *Journal of Petroleum Science and Engineering*, 157: 131-147. https://doi.org/10.1016/j.petrol.2017.06.074

Buades, A., Coll, B. and Morel, J., 2005. A review of image denoising algorithms, with a new one. *Multiscale Modeling & Simulation*, 4(2): 490-530. https://doi.org/10.1137/040616024

Bulat, A., Yang, J. and Tzimiropoulos, G., 2018. To learn image super-resolution, use a gan to learn how to do image degradation first, *Proceedings of the European conference on computer vision (ECCV)*, pp. 185-200.

Cao, J. and Wu, S., 2017. Deep Learning: Chance and Challenge for Deep Gas Reservoir

*IdentificationInternational Geophysical Conference, Qingdao, China, 17-20 April 2017*, pp. 711-712. https://doi.org/10.1190/IGC2017-180

Chen, W., Yu, Y., Shen, Y., Zhang, Z. and Vesselinov, V., 2019. Automatic Drilling Dynamics Interpretation Using Deep Learning, *SPE Annual Technical Conference and Exhibition*. Society of Petroleum Engineers. https://doi.org/10.2118/195919-MS

Elbakri, I.A. and Fessler, J.A., 2002. Statistical image reconstruction for polyenergetic X-ray computed tomography. *IEEE transactions on medical imaging*, 21(2): 89-99. doi: 10.1109/42.993128

Feng, J. et al., 2019a. Reconstruction of porous media from extremely limited information using conditional generative adversarial networks. *Physical Review E*, 100(3): 033308. https://doi.org/10.1103/PhysRevE.100.033308

Feng, J. et al., 2019b. Accurate and fast reconstruction of porous media from extremely limited information using conditional generative adversarial network. *arXiv preprint* arXiv:1905.02135.

Gecer, B. et al., 2019. Synthesizing coupled 3d face modalities by trunk-branch generative adversarial networks. *arXiv preprint* arXiv:1909.02215.

Gecer, B., Ploumpis, S., Kotsia, I. and Zafeiriou, S., 2019. Ganfit: Generative adversarial network fitting for high fidelity 3d face reconstruction, *Proceedings of the IEEE Conference on Computer Vision and Pattern Recognition*, pp. 1155-1164.

Goodfellow, I. et al., 2014. Generative adversarial nets, *Advances in neural information processing systems*, pp. 2672-2680.

Guan, K., 2018. Reconstructing Pore Networks Using Generative Adversarial Networks. http://cs229.stanford.edu/proj2018/report/222.pdf

Gulli, A. and Pal, S., 2017. Deep learning with Keras. *Packt Publishing Ltd*.

Hermoza, R. and Sipiran, I., 2018. 3D Reconstruction of incomplete archaeological objects using a generative adversarial network. *Proceedings of Computer Graphics International 2018*, pp. 5-11. https://doi.org/10.1145/3208159.3208173

Imamverdiyev, Y. and Sukhostat, L., 2019. Lithological facies classification using deep convolutional neural network. Journal of Petroleum Science and Engineering, 174: 216-228. https://doi.org/10.1016/j.petrol.2018.11.023

Izadi, H. et al., 2017. Application of full set of two point correlation functions from a pair of 2D cut sections for 3D porous media reconstruction. Journal of Petroleum Science and Engineering, 149: 789-800. https://doi.org/10.1016/j.petrol.2016.10.065

Jia, C., 2017. Breakthrough and significance of unconventional oil and gas to classical petroleum geology theory - ScienceDirect. Petroleum Exploration and Development, 44(1): 1-10. https://doi.org/10.1016/S1876-3804(17)30002-2

Jia, Y. et al., 2014. Caffe: Convolutional architecture for fast feature embedding, *Proceedings of the 22nd ACM international conference on Multimedia*, pp. 675-678. https://doi.org/10.1145/2647868.2654889

Keehm, Y., Mukerji, T. and Nur, A., 2004. Permeability prediction from thin sections: 3D reconstruction and Lattice-Boltzmann flow simulation. *Geophysical Research Letters*, 31(4). https://doi.org/10.1029/2003GL018761

Lei, Y., 2020. Reconstruction and Analysis of Tight Sandstone Digital Rock Combined with X-Ray CT Scanning and Multiple-Point Geostatistics Algorithm. *Mathematical Problems in Engineering*, 2020. https://doi.org/10.1155/2020/9476060

Li, H., Zheng, Y., Wu, X. and Cai, Q., 2019. 3D model generation and reconstruction using

conditional generative adversarial network. *International Journal of Computational Intelligence Systems*, 12(2): 697-705. https://doi.org/10.2991/ijcis.d.190617.001

Li, P., Zheng, M., Bi, H., Wu, S. and Wang, X., 2017. Pore throat structure and fractal characteristics of tight oil sandstone: a case study in the Ordos Basin, China. *Journal of Petroleum Science and Engineering*, 149: 665-674. https://doi.org/10.1016/j.petrol.2016.11.015

Li, Y., Sun, R. and Horne, R., 2019. Deep learning for well data history analysis, *SPE Annual Technical Conference and Exhibition*. Society of Petroleum Engineers. https://doi.org/10.2118/196011-MS

Liu, S. et al., 2019. A case study on homogeneous and heterogeneous reservoir porous media reconstruction by using generative adversarial networks. *Energy Procedia*, 158: 6164-6169. https://doi.org/10.1016/j.egypro.2019.01.493

Ma, J., Yu, W., Liang, P., Li, C. and Jiang, J., 2019. FusionGAN: A generative adversarial network for infrared and visible image fusion. *Information Fusion*, 48: 11-26. https://doi.org/10.1016/j.inffus.2018.09.004

Mirza, M. and Osindero, S., 2014. Conditional generative adversarial nets. *arXiv preprint* arXiv:1411.1784.

Mosser, L., Dubrule, O. and Blunt, M.J., 2017. Reconstruction of three-dimensional porous media using generative adversarial neural networks. *Physical review. E*, 96(4): 043309-043309. https://doi.org/10.1103/PhysRevE.96.043309

Mosser, L., Dubrule, O. and Blunt, M.J., 2018. Conditioning of three-dimensional generative adversarial networks for pore and reservoir-scale models. *arXiv preprint* arXiv:1802.05622.

Noshi, C.I. and Schubert, J.J., 2018. The role of machine learning in drilling operations; a review, *SPE/AAPG Eastern Regional Meeting*. Society of Petroleum Engineers. https://doi.org/10.2118/191823-18ERM-MS

Øren, P. and Bakke, S., 2002. Process based reconstruction of sandstones and prediction of transport properties. *Transport in porous media*, 46(2-3): 311-343.

Ouellette, M. et al., 2015. Rock Core Analysis: Metallic Core Holders for Magnetic Resonance Imaging Under Reservoir Conditions. *In Mobile NMR and MRI*, pp. 290-309.

Paszke, A. et al., 2017. Automatic differentiation in pytorch. *31st Conference on Neural Information Processing Systems (NIPS 2017)*, Long Beach, CA, USA.

Radford, A., Metz, L. and Chintala, S., 2015. Unsupervised representation learning with deep convolutional generative adversarial networks. *arXiv preprint* arXiv:1511.06434.

Shams, R., Masihi, M., Boozarjomehry, R.B. and Blunt, M.J., 2020. Coupled generative adversarial and auto-encoder neural networks to reconstruct three-dimensional multi-scale porous media. *Journal of Petroleum Science and Engineering*, 186: 106794. https://doi.org/10.1016/j.petrol.2019.106794

Valsecchi, A., Damas, S., Tubilleja, C. and Arechalde, J., 2020. Stochastic reconstruction of 3D porous media from 2D images using generative adversarial networks. *Neurocomputing*. 399, 227-236. https://doi.org/10.1016/j.neucom.2019.12.040

Volkhonskiy, D. et al., 2019. Reconstruction of 3d porous media from 2d slices. *arXiv preprint* arXiv:1901.10233.

Wang, F., Yang, K., You, J. and Lei, X., 2019. Analysis of pore size distribution and fractal dimension in tight sandstone with mercury intrusion porosimetry. *Results in Physics*, 13: 102283. https://doi.org/10.1016/j.rinp.2019.102283

Wang, H., Qin, Z. and Wan, T., 2018. Text generation based on generative adversarial nets with

latent variables, *Pacific-Asia Conference on Knowledge Discovery and Data Mining*. Springer, pp. 92-103.

Wu, K., Nunan, N., Crawford, J.W., Young, I.M. and Ritz, K., 2004. An efficient Markov chain model for the simulation of heterogeneous soil structure. *Soil Science Society of America Journal*, 68(2): 346-351. https://doi.org/10.2136/sssaj2004.3460

Yao, J. et al., 2013. Characteristics of tight oil in Triassic Yanchang formation, Ordos Basin. *Petroleum Exploration and Developmen*t, 40(2): 161-169. https://doi.org/10.1016/S1876-3804(13)60019-1

Yao, J., Wang, C., Yang, Y., Hu, R. and Wang, X., 2013. The construction of carbonate digital rock with hybrid superposition method. *Journal of Petroleum Science and Engineering*, 110: 263-267. https://doi.org/10.1016/j.petrol.2013.10.005

Yeong, C. and Torquato, S., 1998. Reconstructing random media. *Physical review E*, 57(1): 495. https://doi.org/10.1103/PhysRevE.57.495

Yuan, H., Lee, J.H. and Guilkey, J.E., 2010. Stochastic reconstruction of the microstructure of equilibrium form snow and computation of effective elastic properties. *Journal of Glaciology*, 56(197): 405-414. https://doi.org/10.3189/002214310792447770

Zhang, X.P. and Desai, M.D., 2002. Wavelet based automatic thresholding for image segmentation, *Proceedings of International Conference on Image Processing*. Vol. 1, pp. 224-227. dio: 10.1109/ICIP.1997.647744

Zhou, T., Liu, W., Zhou, C. and Chen, L., 2018. Gan-based semi-supervised for imbalanced data classification, 2018 4th International Conference on Information Management (ICIM). IEEE, pp. 17-21. dio: 10.1109/INFOMAN.2018.8392662

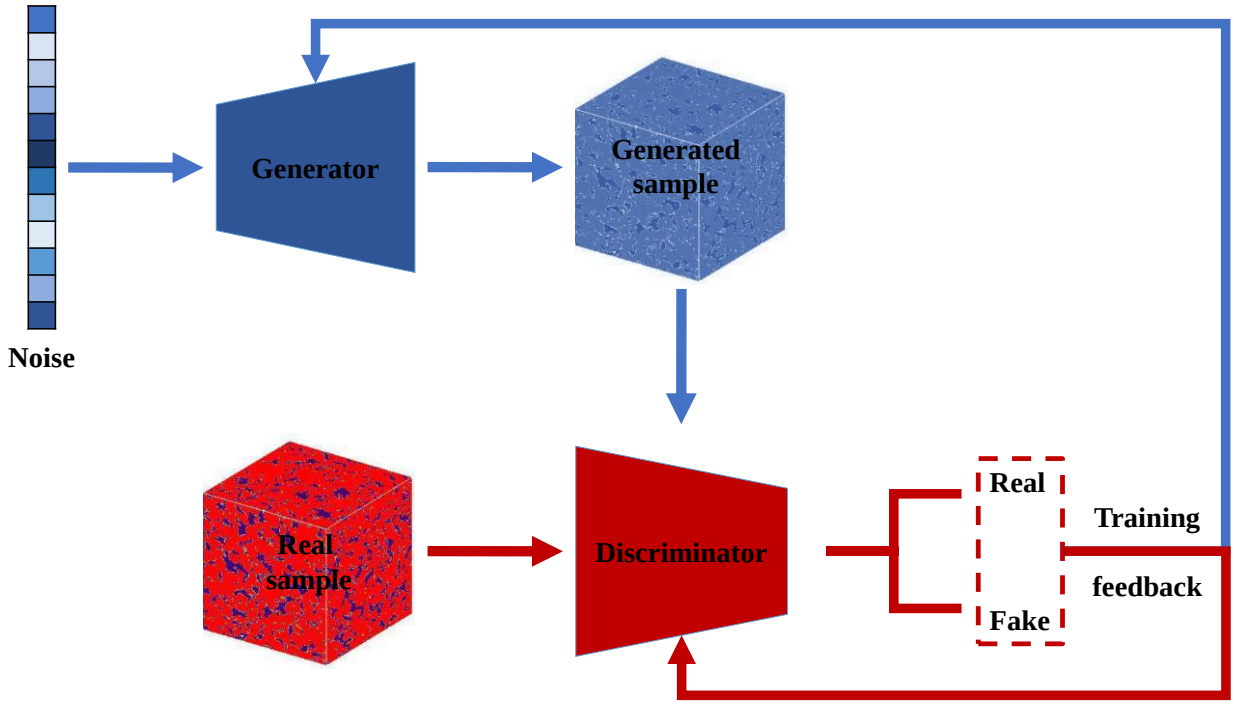


**Figure 1** The schematic diagram of 3D digital rock reconstruction with DCGAN.

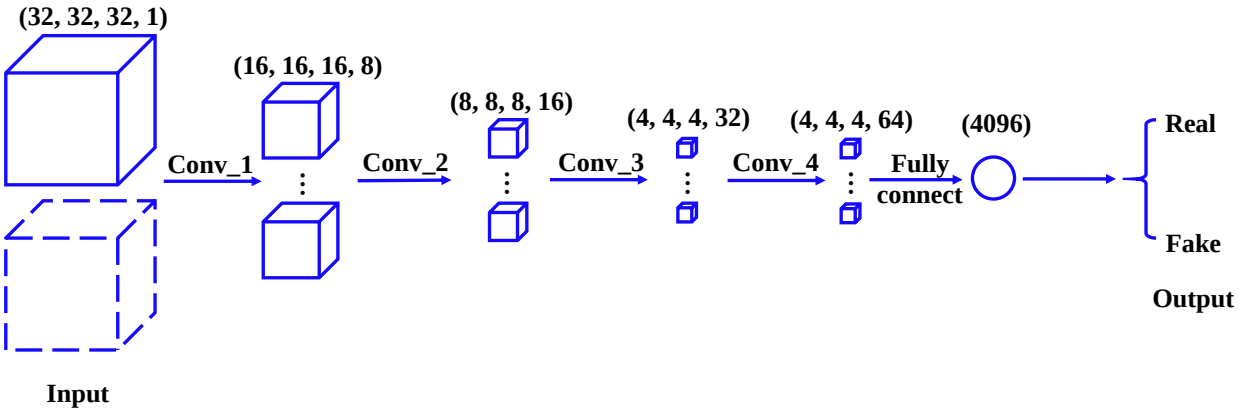


**Figure 2** The structure of discriminator.

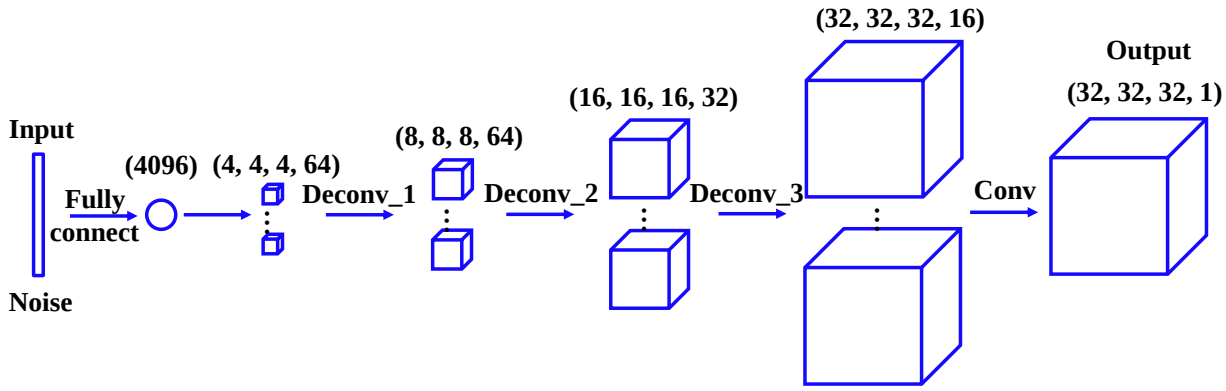


**Figure 3** The structure of generator

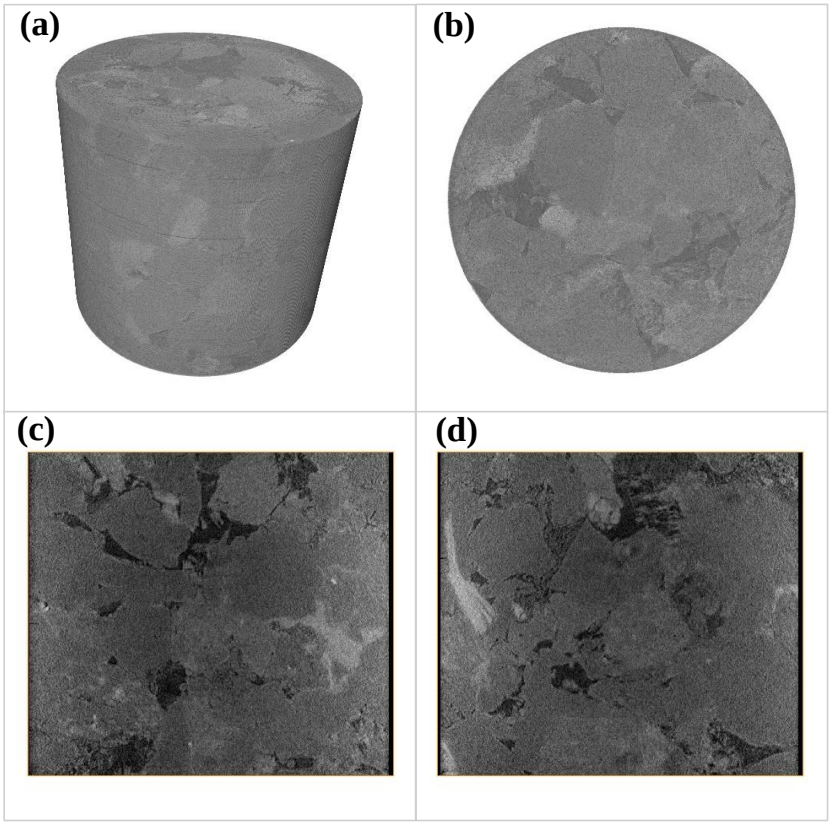


**Figure 4** CT images of tight sandstones from Yanchang formation, Ordos Basin, NW China ((a) 3D view of core samples, (b) CT slice in XY direction, (c) CT slice in XZ direction, (d) CT slice in YZ direction)

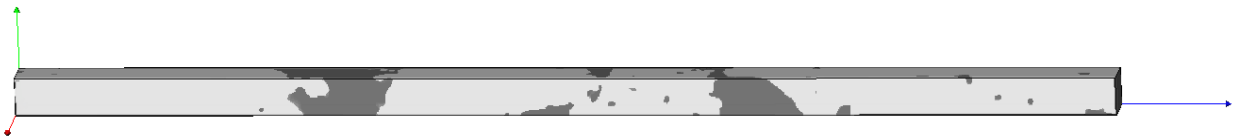

**Figure 5** The binary CT images of tight sandstones for training, and the size of images are 32×32×910.

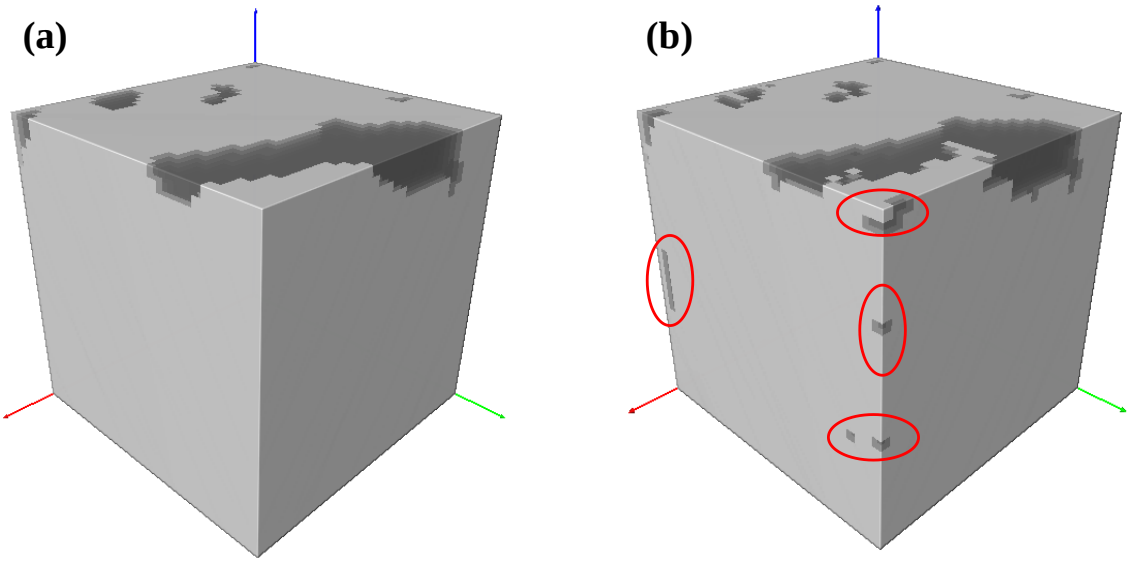


**Figure 6** Comparison of the original digital rock (a) and the generated digital rock reconstructed by deep learning (b)

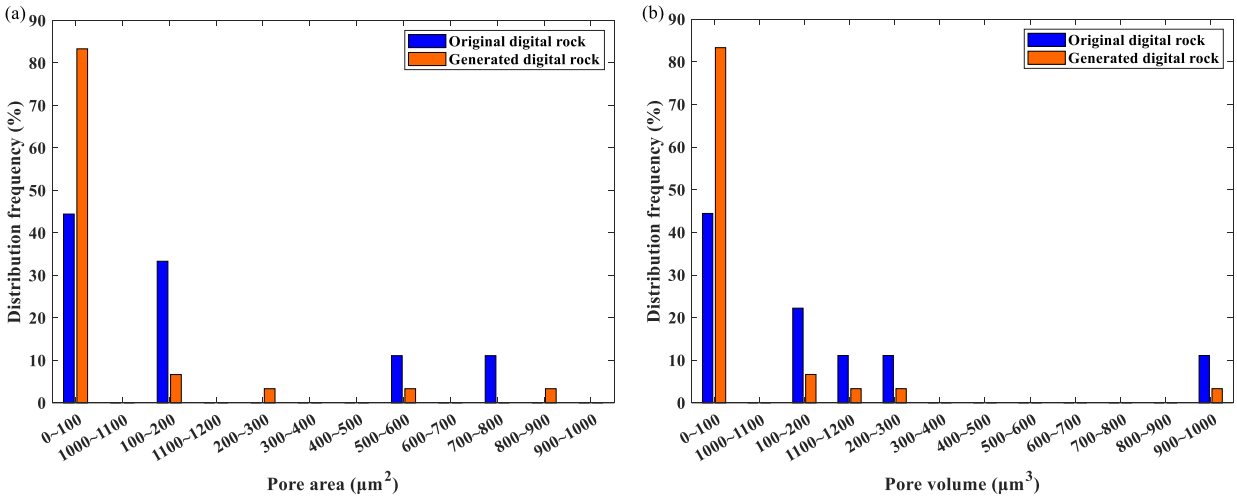


**Figure 7** Comparison of the pore area (a) and pore volume (b) in the original digital rock

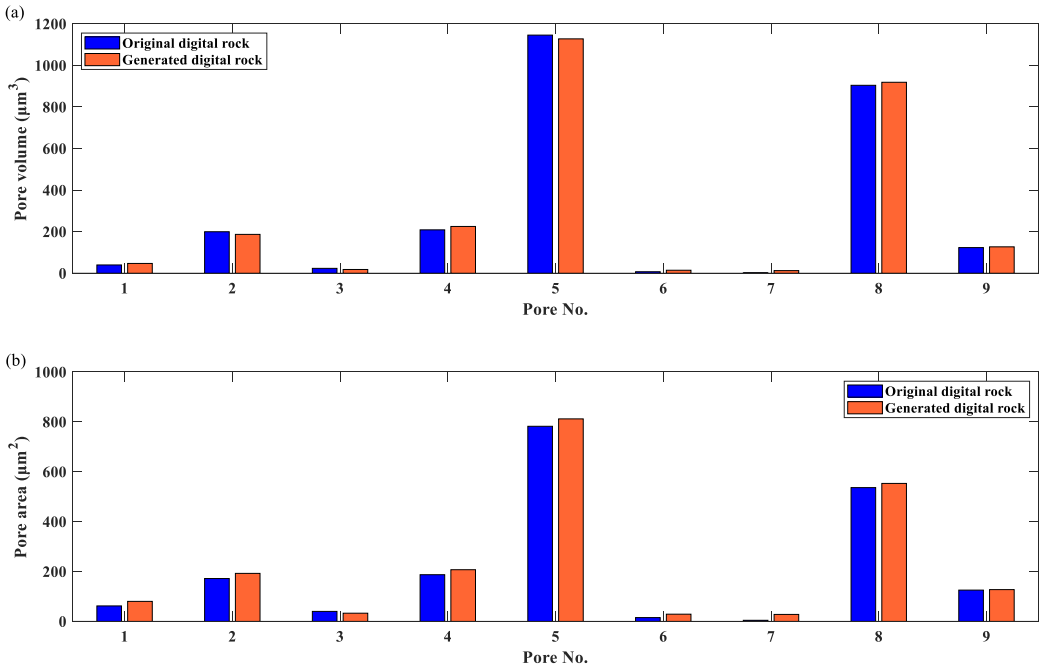


**Figure 8** Comparison of pore volume (a) and pore area (b) in the original digital rock and generated digital rock

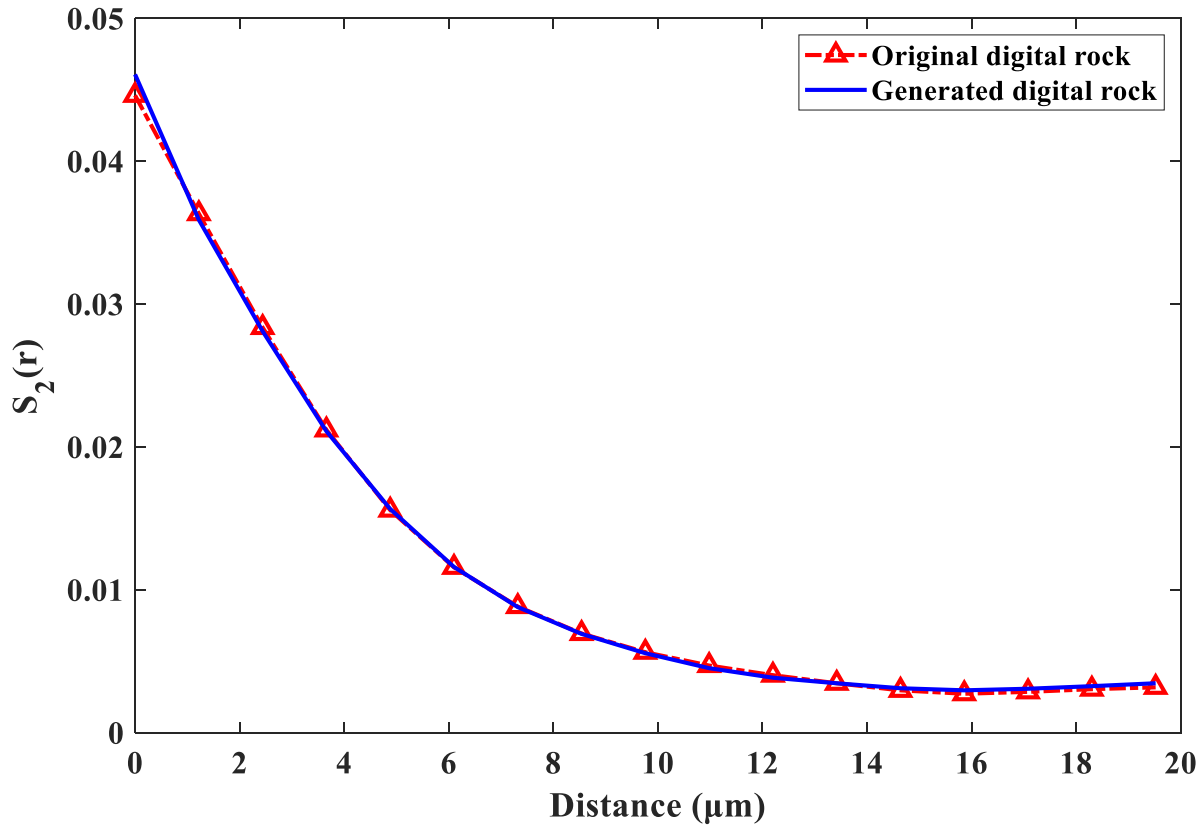


419

420 **Figure 9** Two-point probability function of the original digital rock and the generated digital
421 rock after denoising.
422

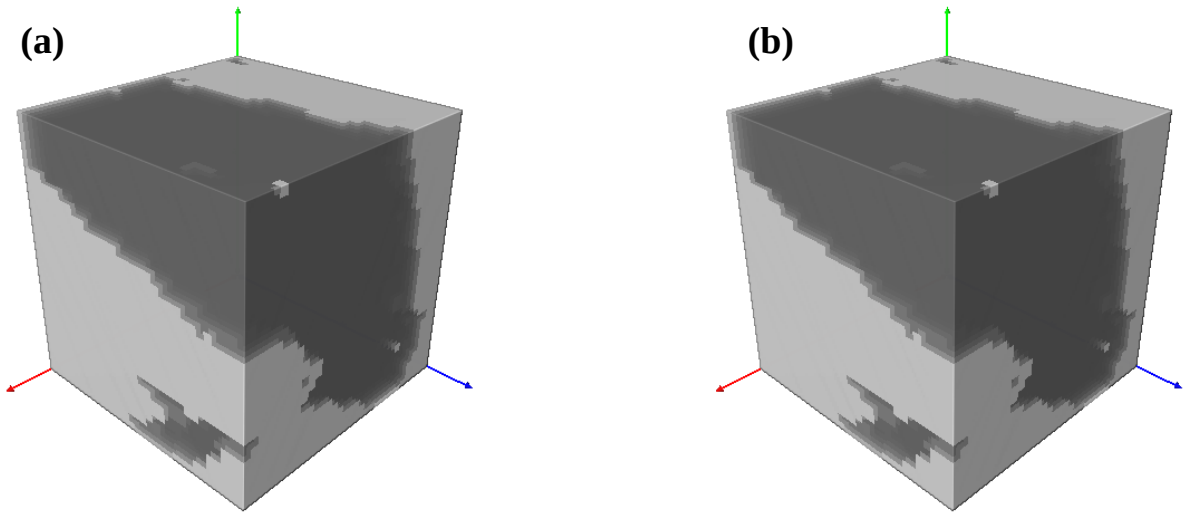


**Figure 10** The original 3D digital rock (a) and the generated 3D digital rock reconstructed by deep learning (b)

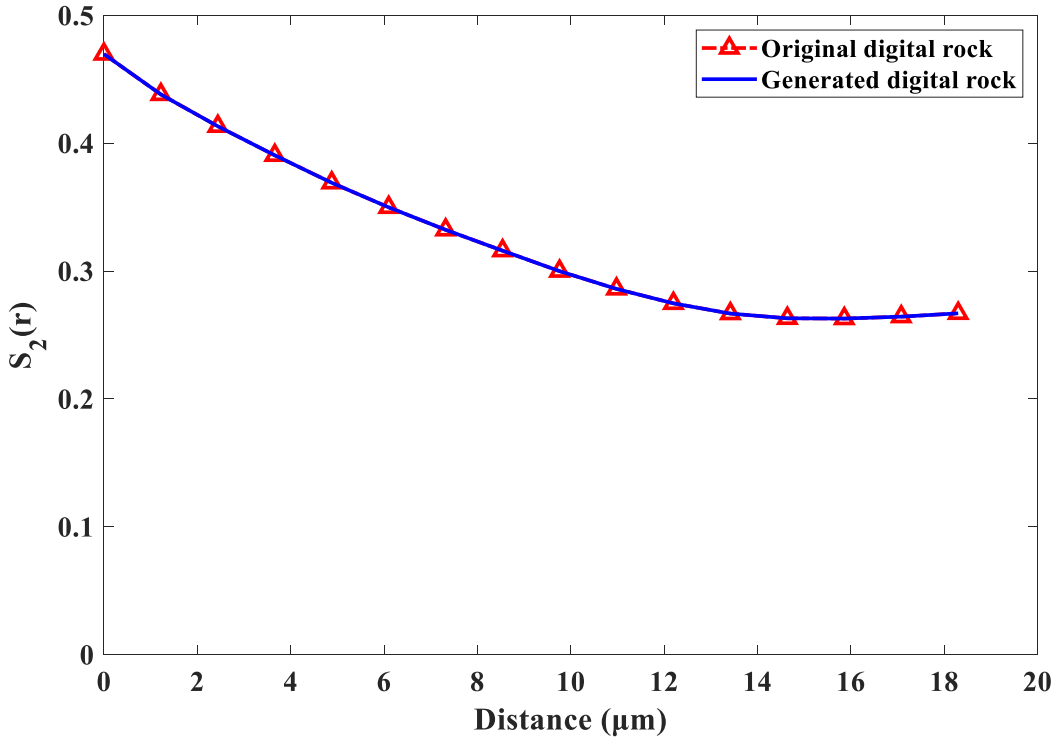


427

428 **Figure 11** Two-point probability function of the original digital rock and the generated digital
429 rock reconstructed by DCGAN.

430

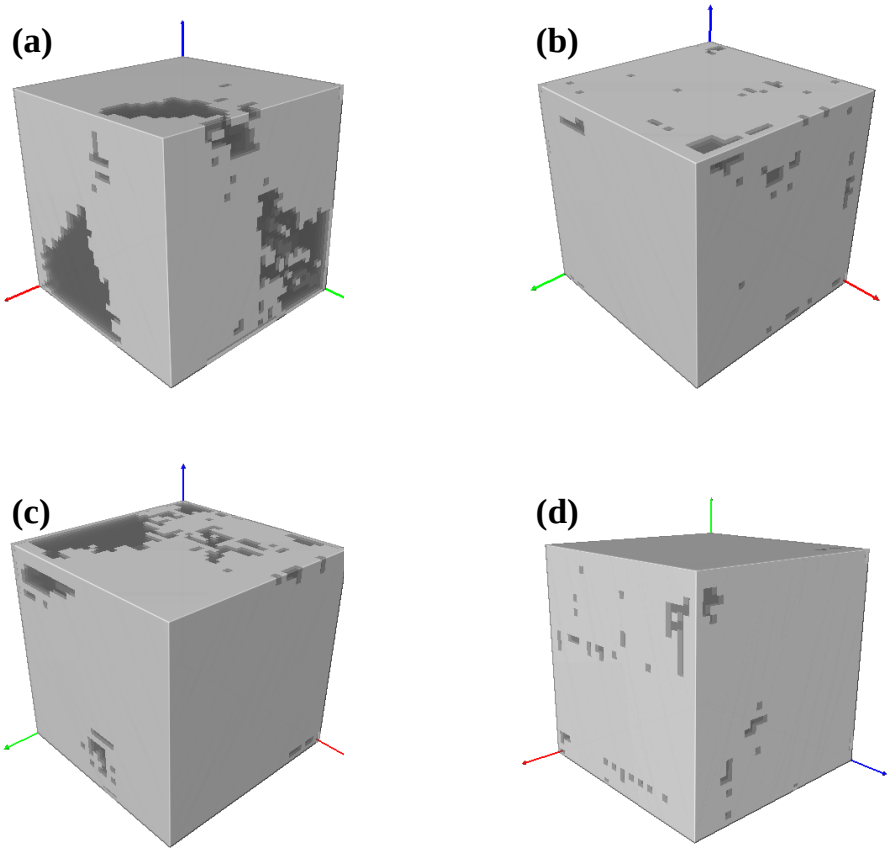


**Figure 12** Four generated 3D digital rock reconstructed by DCGAN.

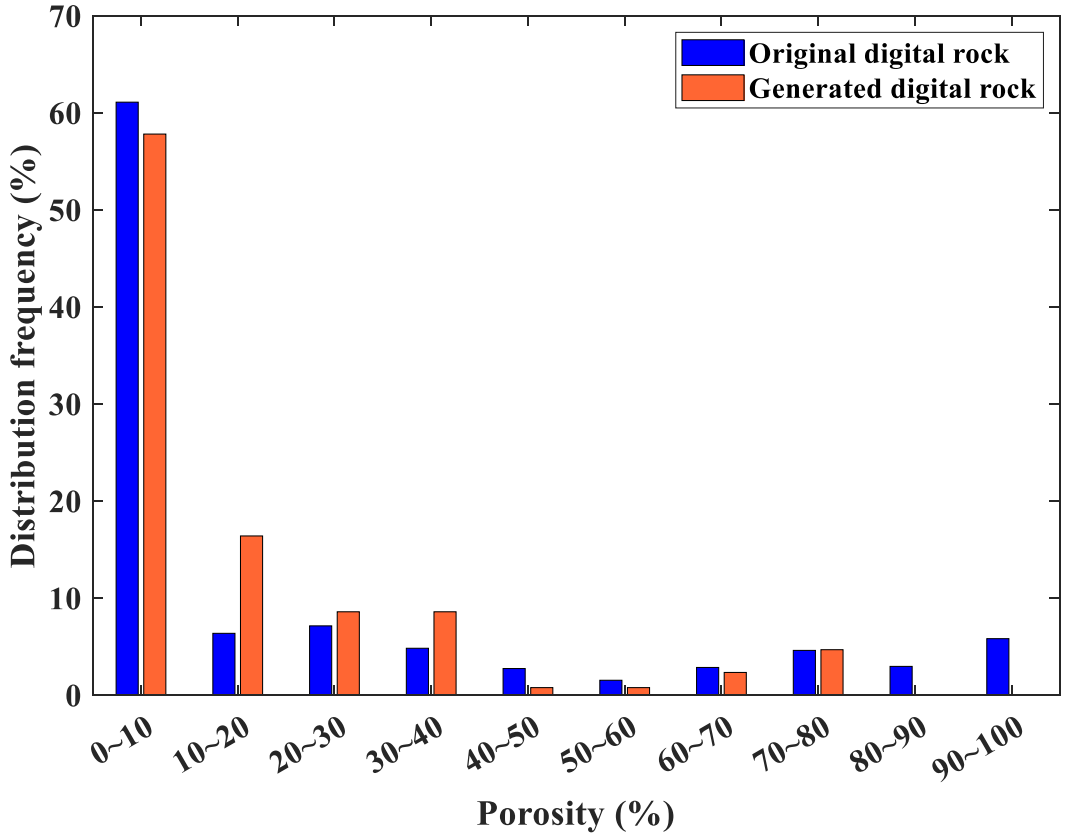


434

435 **Figure 13** Comparison of porosity distribution between original digital rock and the generated
436 digital rock.
437

438 **Table 1** the parameter of DAGAN for 3D digital rock reconstruction

| Layer | | Type | Filter number | Kernel | Stride | Padding | Batchnor-malization | Dropout | Activation |
|---|---|---|---|---|---|---|---|---|---|
| Generator | 1 | Deconv | 64 | 2×2×2 | 2 | same | Yes | 0 | ReLU |
| | 2 | Deconv | 32 | 2×2×2 | 2 | same | Yes | 0 | ReLU |
| | 3 | Deconv | 16 | 2×2×2 | 2 | same | Yes | 0 | ReLU |
| | 4 | Conv | 1 | 3×3×3 | 1 | same | Yes | 0 | tanh |
| Discriminator | 1 | Conv | 8 | 3×3×3 | 2 | same | Yes | 0.25 | Leaky ReLU |
| | 2 | Conv | 16 | 3×3×3 | 2 | same | Yes | 0.25 | Leaky ReLU |
| | 3 | Conv | 32 | 3×3×3 | 2 | same | Yes | 0.25 | Leaky ReLU |
| | 4 | Conv | 64 | 3×3×3 | 1 | same | Yes | 0.25 | Leaky ReLU |
| | 5 | Fully Connect | 4096 | - | - | - | - | - | Sigmoid |

439

**Table 2** Comparison of barycenter coordinates of the pores in the original digital rock and generated digital rock.

| Pore no. | Original digital rock | | | Generated digital rock | | | Euclidean distance (μm) |
|---|---|---|---|---|---|---|---|
| | Barycenter coordinate X (μm) | Barycenter coordinate Y (μm) | Barycenter coordinate Z (μm) | Barycenter coordinate X (μm) | Barycenter coordinate Y (μm) | Barycenter coordinate Z (μm) | |
| 1 | 0.83 | 0.55 | 1.94 | 0.99 | 0.52 | 3.28 | 1.35 |
| 2 | 11.67 | 2.36 | 2.04 | 11.74 | 2.36 | 2.17 | 0.15 |
| 3 | 36.60 | 0.94 | 1.97 | 36.23 | 0.85 | 1.83 | 0.40 |
| 4 | 20.77 | 10.69 | 2.78 | 20.99 | 10.82 | 2.63 | 0.29 |
| 5 | 15.93 | 31.85 | 1.56 | 16.16 | 31.83 | 1.60 | 0.24 |
| 6 | 35.69 | 26.54 | 0.31 | 28.82 | 22.42 | 13.88 | 15.76 |
| 7 | 2.44 | 1.22 | 18.30 | 0.00 | 1.22 | 20.74 | 3.45 |
| 8 | 6.28 | 23.41 | 32.04 | 6.30 | 23.30 | 31.99 | 0.13 |
| 9 | 21.62 | 3.36 | 35.49 | 21.70 | 3.35 | 35.48 | 0.08 |

**Table 3** The barycenter coordinates of the pores in the original digital rock and generated digital rock.

| Label | Original digital rock | | | Generated digital rock | | | Euclidean distance (μm) |
|---|---|---|---|---|---|---|---|
| | Barycenter coordinate X (μm) | Barycenter coordinate Y (μm) | Barycenter coordinate Z (μm) | Barycenter coordinate X (μm) | Barycenter coordinate Y (μm) | Barycenter coordinate Z (μm) | |
| 1 | 2.00 | 0.80 | 1.40 | 2.00 | 0.80 | 1.40 | 0.00 |
| 2 | 9.60 | 0.00 | 0.00 | 9.60 | 0.00 | 0.00 | 0.00 |
| 3 | 21.58 | 17.21 | 20.35 | 21.58 | 17.21 | 20.35 | 0.00 |
| 4 | 12.00 | 1.20 | 0.00 | 12.00 | 1.20 | 0.00 | 0.00 |
| 5 | 7.60 | 4.40 | 0.00 | 7.60 | 4.40 | 0.00 | 0.00 |
| 6 | 0.00 | 5.60 | 0.40 | 0.00 | 5.60 | 0.40 | 0.00 |
| 7 | 3.60 | 6.00 | 0.00 | 3.60 | 6.00 | 0.00 | 0.00 |
| 8 | 0.00 | 9.60 | 0.60 | 0.00 | 9.60 | 0.60 | 0.00 |
| 9 | 2.40 | 9.60 | 0.60 | 2.40 | 9.60 | 0.60 | 0.00 |
| 10 | 8.40 | 3.60 | 6.00 | 8.40 | 3.60 | 6.00 | 0.00 |
| 11 | 31.20 | 24.00 | 12.00 | 31.20 | 24.00 | 12.00 | 0.00 |
| 12 | 27.60 | 25.20 | 37.20 | 27.60 | 25.20 | 37.20 | 0.00 |